Microdeformation and Fracture Mechanisms in Polyamide-6/ Organoclay Nanocomposites

Chaobin He,[†] Tianxi Liu,[†] Wuiwui Chauhari Tjiu,[†] Hung-Jue Sue,[‡] and Albert F. Yee*[,§]

Institute of Materials Research and Engineering, 3 Research Link, Singapore 117602; Department of Mechanical Engineering, Texas A&M University, College Station, Texas 77843-3123; and Department of Chemical Engineering and Materials Science, University of California, Irvine, Irvine, California 92697-2575

Received August 7, 2007; Revised Manuscript Received October 31, 2007

ABSTRACT: A study on the mechanisms for embrittlement of polyamide-6 (PA-6) by nanometer-sized clay in nanocomposites is reported in this paper. Tensile modulus and yield strength in these composites were found to increase with clay concentration, while the strain at rupture decreased. Similar to the strain at rupture, fracture toughness also decreased dramatically. Investigation by transmission electron microscopy alone indicates that multiple crazing appears to be the only significant toughening mechanism for the nanocomposite with 2.5 wt % clay which does not explain why composites with more clay are significantly more brittle. The deformation behavior was therefore further studied using wide (WAXS) and small (SAXS) angle X-ray scattering, scanning electron microscopy (SEM), and optical microscopy. WAXS detected the existence of the γ-phase of PA-6, probably due to the presence of clay. However, the occurrence of this crystalline phase cannot explain the observed changes in mechanical behavior. SAXS study indicated that crazing occurred in the PA-6 matrix in tension and that the craze concentration depended on clay loading. The highest craze concentration was observed at 2.5 wt % clay. The existence of crazes in nanoclay composites was also confirmed by optical microscopy and transmission electron microscopy. In addition, SAXS showed that microcracking also occurred in these nanocomposites along with crazing, with the highest concentration of microcracks observed at 2.5 wt % clay loading. TEM showed that microcracks occurred near the interface of clay and matrix. The existence of a high concentration of crazes and microcracks in the nanocomposite with 2.5 wt % of clay is the likely cause for its high toughness relative to those composites containing higher clay loading. At higher clay loadings the high incidence of microcracks probably prevented the crazing mechanism from operating to its fullest possible extent, thus resulting in low toughness.

1. Introduction and Objectives

Polymer/clay nanocomposites—a class of reinforced plastics formed by dispersing nanosized clay particles throughout a polymer matrix—have received much attention in both academic and industrial arenas due to their enhanced mechanical[1,2] and barrier[3,4] properties and flame resistance.[5] Extensive efforts have been devoted to the development and characterization of such nanocomposites.[6−12] Yet, the mechanisms responsible for the degradation in toughness, a common observation in these materials, have not been fully identified.

Polyamide-6 (PA-6)-based clay nanocomposites were first studied by a Toyota research group.[13−15] Many subsequent investigations have focused on preparation and macroscopic mechanical property characterization,[10,11,16−19] on the influences of clay addition to crystalline structure and morphology of PA-6,[20−22] on thermal properties,[23−25] and on rheology.[26,27] There has been general agreement that polymer-based clay nanocomposites are much more brittle than their neat polymer counterparts,[10,13,16] which severely limits their use in load-bearing applications.[19,28,29] The fundamental causes for embrittlement are still unclear; consequently, it is imperative that they be sought to allow effective toughening of polymer nanocomposites to render them suitable for structural applications.

The objective of the present work is to detail the microdeformation and fracture mechanisms in a series of PA-6/clay nanocomposites using X-ray scattering and microscopy techniques that produce new results not heretofore reported. It is hoped that these will help explain why nanoparticles nearly always embrittle otherwise ductile polymers. Also reported are more conventional wide-angle X-ray scattering and tensile stress−strain behavior results. The objective of these latter experiments is primarily to show that the materials studied in this work are exfoliated to extents similar to those already studied and reported by others[10−22] and that the matrix crystallinity and macroscopic properties are also similar. No attempt is made in the present work to investigate why certain types of crystal polymorphs appear, nor how much the crystallinity has changed and how that might contribute to the modulus, etc.; however, the role of crystallinity on possible changes in the *mode* of deformation is briefly explored. Similarly, no attempt is made to fit the stress−strain behavior to continuum models of composites or plasticity because to do so would go beyond the scope of this investigation.

2. Experimental Section

2.1. Materials. PA-6 (SF1080A) used in this study is a product of Ube Industries. The unmodified pristine clay (montmorillonite) and modified organoclay (Nanomer I.30TC) were supplied by Nanocor Inc. All the samples were dried in a vacuum oven at 80 °C for 24 h before mixing. PA-6/clay nanocomposites containing 0, 2.5, 5, 7.5, and 10 wt % organoclay were prepared via melt-compounding using a Brabender twin-screw extruder at 250 °C, with screw speeds of 80−100 rpm. Henceforth in this paper, all

* To whom correspondence should be addressed.
[†] Institute of Materials Research and Engineering.
[‡] Texas A&M University.
[§] University of California, Irvine.

10.1021/ma071781s CCC: $40.75
Published on Web 12/08/2007

mention of PA-6/clay nanocomposites shall refer to the use of the modified organoclay unless otherwise specified, and "*xx*" in PA-6/*xx* shall refer to the weight percentage of clay in the nanocomposite.

2.2. Specimen Preparation. The extrusion compounded nanocomposite pellets were injection-molded with a Battenfeld 300 CD Plus molding machine into tensile bars that have a cross section of 12.7 mm × 3.6 mm and a gauge length of about 100 mm, which conforms to ASTM D638. The barrel temperature was set at 250 °C and the mold temperature at 80 °C. The pellets were also injection-molded into rectangular bars with dimensions of 6 mm × 12.5 mm × 160 mm for single-edge-notch three-point-bending (SEN-3PB) tests.[30] Prior to testing, all specimens were dried in a vacuum oven at 80 °C for 24 h.

2.3. Mechanical Testing. The tensile and bending tests were conducted using an Instron mechanical testing machine (model 5567) at a cross-head speed of 5 mm/min at room temperature. An extensometer (model 2630-105 from Instron) was used to accurately determine the engineering (nominal) tensile strain up to the point where specimen necking began. The tensile tests, data collection, and analyses were carried out following procedures described in ASTM D638. The cross-head speed and specimen combination produces a strain rate of 0.0033 s^{-1}. From the linear portion of the engineering stress−strain curve the Young's modulus was determined.

The SEN-3PB specimens were notched to a depth of 5.5 mm with a notch cutter, followed by tapping in a razor blade that had previously been chilled in liquid nitrogen. This procedure produced a sharp crack, usually to a total crack length a of about 6.5 mm ($a/W = 0.45-0.55$, where W is the depth of the specimen) for SEN-3PB tests.[30] It will be shown in the Results section that these geometries produced linear load-deflection curves in all but the pure PA-6 specimens.

Double-notch four-point-bending (DN-4PB) specimens were also prepared in order to study crack tip damage mechanisms in a subcritically propagated crack.[31] In these specimens two nearly identical cracks were prepared with care.

2.4. WAXS/SAXS. Wide-angle X-ray scattering (WAXS) was performed with a Bruker X-ray diffractometer fitted with a 2-D detector, using nickel-filtered Cu $K\alpha_1$ radiation source (λ = 0.154 18 nm) at 40 kV and with a current of 40 mA. Testing was carried out with 2θ scanned between 1.5° and 30° at a scanning rate of 1°/min. Small-angle X-ray scattering (SAXS) was performed on a Bruker Nanostar small angle diffractometer, using Cu $K\alpha_1$ radiation source (λ = 0.154 18 nm). The SAXS data were first subtracted from background scattering and then divided by detector response. The scattering position was calibrated using the rattail standard.

2.5. Microscopy. The fine scale dispersion of nanoclay platelets and the initiation and development of crazes in these nanocomposites were observed using a Philips FEG-CM300 transmission electron microscope (TEM) at the accelerating voltage of 200 kV. Thin sections having a thickness of 70 nm were cut for TEM observation from the midsections of injection-molded bars using a Leica ultramicrotome equipped with a diamond knife under cryogenic cooling. The fracture surfaces of PA-6 and its nanocomposites from the SEN-3PB tests were observed using a scanning electron microscope (JEOL-JSM-5600 SEM) at the accelerating voltage of 5 kV. Prior to SEM observation, the fracture surfaces were coated with a thin layer of gold. The damage zone region of DN-4PB samples were polished to about 80 μm in thickness. The morphologies of these thin sections were examined using transmission optical microscopy under both bright field and crossed-polar conditions.

3. Results

3.1. Crystal Structure and Morphology of PA-6 Nanocomposite. The nanoplatelets of clay are organized in layers, similar to the structure of smectic liquid crystals.[32,33] This layer arrangement gives rise to low angle scattering in WAXS, where the peak represents the interlayer distance.[34−36] The WAXS patterns for the pristine natural clay, organically modified clay (organoclay), and the PA-6/organoclay nanocomposites are shown in Figure 1.

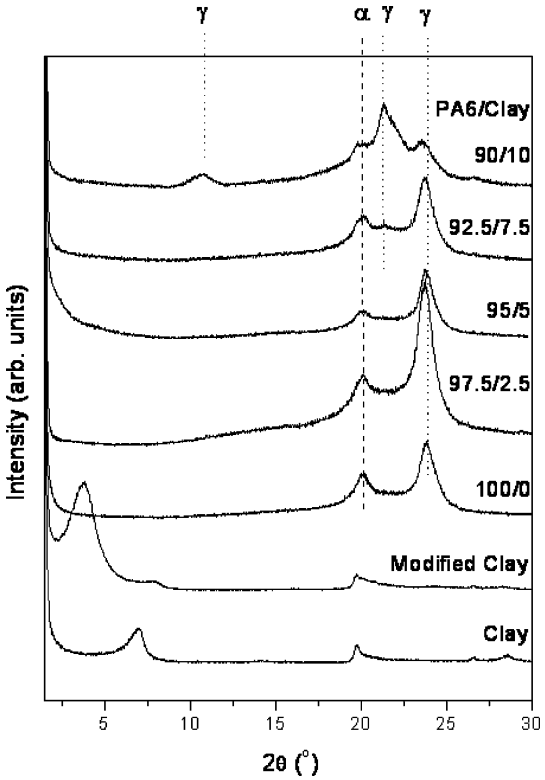

Figure 1. WAXS patterns of pristine and modified clay, PA-6, and PA-6/clay nanocomposites.

The WAXS pattern of the natural clay mineral exhibits a reflection peak at $2\theta = 6.9°$, corresponding to a basal spacing of 1.42 nm. For organoclay, the reflection peak of the basal plane shifts to $2\theta = 4.1°$ with a d-spacing of 2.39 nm, indicating that a swollen and intercalated structure was formed by inserting the surfactant into the gallery of clay platelets. After mixing into PA-6 by the twin-screw extruder, the peak due to the basal plane of organoclay disappears in the XRD patterns for the nanocomposites with different clay loading levels up to 10 wt %. The absence of basal peaks in PA-6/clay nanocomposites suggests the formation of a widely spaced platelet or exfoliated nanostructure. The WAXS results for PA-6/2.5, PA-6/5, PA-6/7.5, and PA-6/10 are shown in Figure 1.[34−36] They are a good indication of successful overall exfoliation although the existence of some remnants of unexfoliated clay cannot be ruled out from WAXS experiments. The TEM (Figure 2) also suggests that the majority of clay particles had been exfoliated in the PA-6 matrix. In this micrograph the clay platelets appear as distinct dark lines dispersed in the polymer matrix. Furthermore, injection-molding process-induced clay orientation can be clearly observed, especially near the specimen surface, where this TEM specimen was obtained. These results are similar to those reported in the literature.[20,22,37]

The extent of exfoliation and dispersion of the clay in these nanocomposites was also investigated using SAXS. Figures 3 and 4 are SAXS of neat PA-6 and PA-6/2.5. Both sets of results are dominated by a scattering peak at $q \sim 0.08$ Å^{-1} ($q = 4\pi \sin \theta/\lambda$), which corresponds to a d-spacing of 8 nm. This scattering peak can be regarded as being from the crystalline lamellar structure, and the position of the scattering peak represents the lamellar thickness. Except for this peak, there is

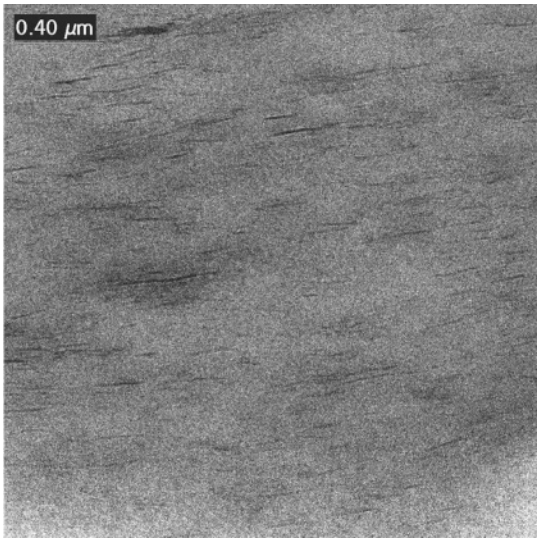

Figure 2. Bright field TEM micrograph showing exfoliated clay in PA-6/2.5. The specimen was prepared by injection-molding. The injection direction is approximately horizontal.

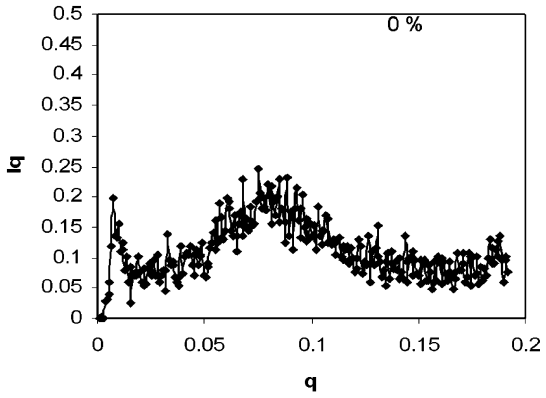

Figure 3. SAXS of neat PA-6, where $q = 4\pi \sin(\theta)/\lambda$ (1/Å) and $I =$ counts/s.

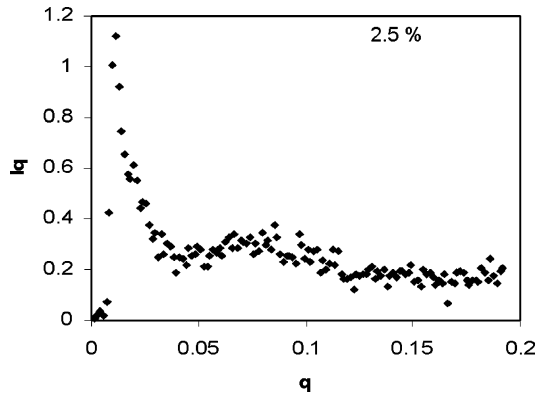

Figure 4. SAXS of PA-6/2.5 nanocomposite after fracturing in tension at cross-head speed of 2.5 mm/min, where $q = 4\pi \sin(\theta)/\lambda$ (1/Å) and $I =$ counts/s.

no significant scattering peak in SAXS up to 80 nm for the PA-6 nanocomposite, indicating that in these materials the concentration of aggregates with a dimension up to 80 nm is too low to give rise to X-ray scattering. The strong low angle scattering observed in the nanocomposite can be attributed to the scattering tail from exfoliated clay, which has dimensions of approximately 100 nm × 100 nm × 1 nm.

3.2. Effect of Clay on the Crystal Structure of PA in the Nanocomposite. PA-6 is a semicrystalline polymer with a rather complex crystalline structure. It is known that PA-6 exhibits three crystalline forms that generally coexist in various amounts.[21,38] The stable monoclinic α-form has a planar zigzag chain conformation, with the H-bonds lying between antiparallel chains, within (002) planes. The monoclinic γ form has a chain twist in the amide groups with respect to the methylene segment so that the monomer unit is in a T_4STS (T = trans; S = skew) conformational sequence that slightly shortens the crystallographic chain axis. The H-bonds link parallel chains within (200) planes, and the H-bonded sheets display a regular up and down displacement. The metastable pseudohexagonal β-form is not as well identified, which can be viewed as an intermediate structure between α- and γ-forms from the standpoint of H-bond setting and chain conformation.

A silicate-induced crystal transformation from the α-form to the γ-form of PA-6 is observed by WAXS (Figure 1); i.e., the formation of γ-form crystals is strongly enhanced by the presence of inorganic fillers. With the increase in clay concentration, the population of γ crystals increases while the population of α-crystals decreases. Moreover, the overall crystallinity of the nanocomposite decreases with increasing clay concentration.

3.3. Molecular Weight of Polymer Matrix. Some mechanical properties of polymers strongly depend on the molecular weight of the polymer.[20] For example, the brittle response of a polymeric material sometimes results from excessively low molecular weight. It has been suggested that the incorporation of modified clay into a polymer matrix through melt compounding at a high temperature (~250 °C) may give rise to molecular weight degradation catalyzed by the addition of clay.[39−41] It has been hypothesized further that the yellowish appearance of the resulting nanoclay PA-6 composites is evidence for significant degradation, which could be a cause for the embrittlement.

To determine whether molecular weight degradation occurs due to melt processing, the ideal experiment to perform would be to extract the clay out of the composite and measure the molecular weight of the remnant. However, such an experiment would be exceedingly difficult to perform given the fact that the exfoliated clay is only nanometers in size. Furthermore, the possibility that some polymer molecules remain attached to the large surface area of clay nanoparticles cannot be ruled out, thus rendering complete extraction or separation improbable. Consequently, the comparison was made between two composites of PA-6 and clay—one a simple mixture and the other the melt-compounded nanocomposite—by measuring their respective intrinsic viscosities. The intrinsic viscosity, which is obtained from dilute solution measurements, is known to be particularly sensitive to the high molecular weight fractions of polymers with a molecular weight distribution and thus would be useful for signaling any significant degradation. Consequently, the molecular weights of PA-6 containing 5% clay through melt compounding and physical mixing were determined using the intrinsic viscosity technique with formic acid as the solvent. The results are shown in Table 1.

Table 1. Intrinsic Viscosity [η] of PA-6 in Formic Acid at 25 °C before and after Melt Compounding

polymer system	intrinsic viscosity [η], dL/g	mol wt, g/mol (from Mark−Houwink eq)
PA-6 compounded with 5% organoclay	0.81	NA
PA-6 simply mixed with 5% clay	0.83	NA
neat PA-6	0.82	19200

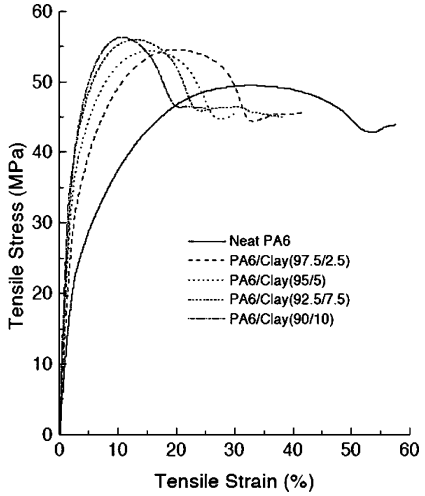

Figure 5. Stress−strain curve for neat PA-6 and PA-6 clay nanocomposites with various clay concentrations.

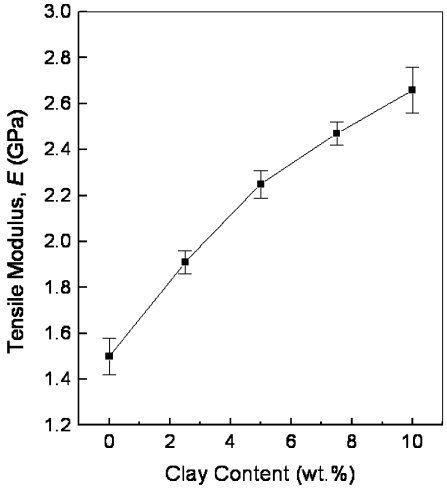

Figure 6. Tensile modulus of PA-6 nanocomposites with various clay concentrations. The error bars indicate one standard deviation. 10−12 specimens were used to obtain each data point.

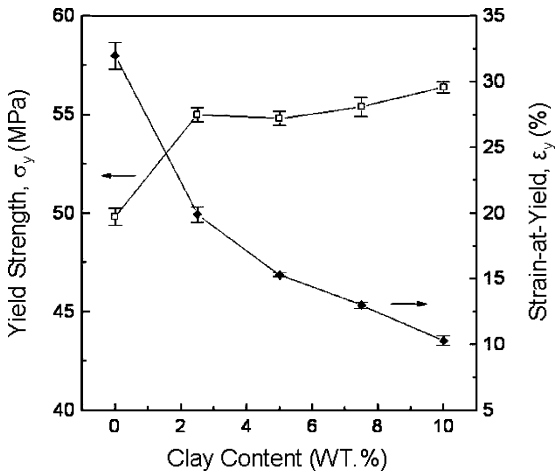

Figure 7. Yield strength (σ_y) and strain at yield (ϵ_y) of PA-6 nanocomposites with various clay concentrations. The error bars indicate one standard deviation. 10−12 specimens were used to obtain each data point.

The intrinsic viscosity, [η], for PA-6 physically mixed with 5% clay is 0.83 dL/g, while for PA-6 melt-compounded with the same amount of clay (exfoliated), [η] = 0.81 dL/g. The intrinsic viscosity for neat PA-6 was also obtained and is included in Table 1 for reference. The difference between the intrinsic viscosity values is within experimental scatter. Given the typical uncertainties in such measurements, it can be suggested that the melt compounding does not significantly degrade the molecular weight of the PA-6 matrix. It might be argued that the large surface area of the nanoparticles of clay *should* have a large influence on the viscosity of the solution, and the similarities in the intrinsic viscosities might be due to offsetting effects. However, any further investigation along this line is beyond the scope of the present research.

3.4. Tensile Properties. The data reported here represent an average of at least six tests. The engineering (nominal) stress−strain curves of the nanocomposites are shown in Figure 5.

The maximum in the engineering stress is taken as the yield strength in accordance with ASTM D638. Note that after the maxima in the stress the materials underwent some necking, and the deformation became localized in the neck. Further extension of the specimen was largely due to extension of the neck. For this reason the data for further extension of the neat PA-6 beyond 60% is not shown in Figure 5 in order to show the data for the nanocomposites with greater clarity. Note that the strain values reported in these curves are nominal and conform to ASTM D638. Consequently, these nominal stress−strain curves cannot be used to compare with continuum mechanics models of composites or plasticity except in the linear region. The tensile modulus is obtained from the initial linear portions of the curves in a low strain range (0.1−1%). It can be seen that as clay concentration increases, both the Young's modulus (Figure 6) and the yield strength (Figure 7) of the nanocomposites increase significantly. The modulus of the nanocomposite containing 5 wt % clay is about 50% higher than that of neat PA-6 (Figure 6). Such high stiffening efficiency has already been reported by other researchers,[20,22,37] and the data presented here are comparable. These results highlight the impressive reinforcement effect of the high aspect ratio exfoliated platelets.[35,42] For the nanocomposite PA-6/2.5, the yield strength is increased (Figure 7) while the engineering strain at break is decreased (Figure 5) from the corresponding values of neat PA-6. And, with further increase in clay content, the yield strength continues to rise (Figure 7), albeit more slowly while the materials fractured at ever decreasing nominal strain at break values (Figure 5). The last observation is one of the motivations for this investigation.

3.5. Fracture Toughness and Fracture Surfaces of SEN-3PB Specimens. The fracture toughness, described as the critical stress intensity factor, K_{IC}, was measured using SEN-3PB specimens. The K_{IC} values were determined using the following relationship:[43,44]

$$K_{IC} = Y\frac{3PS\sqrt{a}}{2BW^2}$$

$$Y = 1.93 - 3.07(a/W) + 14.53(a/W)^2 - 25.11(a/W)^3 + 25.80(a/W)^4$$

where Y is a shape factor, P the load at failure, S the length of the span, B the thickness of the specimen, W the depth of the specimen, and a the crack length. Five to seven specimens were tested for each PA-6/clay nanocomposite system to obtain K_{IC}. Figure 8A shows the load−displacement curves from the SEN-3PB tests. Except for that for neat PA-6, the curves are linear, which is typical for materials that fracture with a small plastic zone. The K_{IC} values calculated using the above equations are presented in Figure 8B.

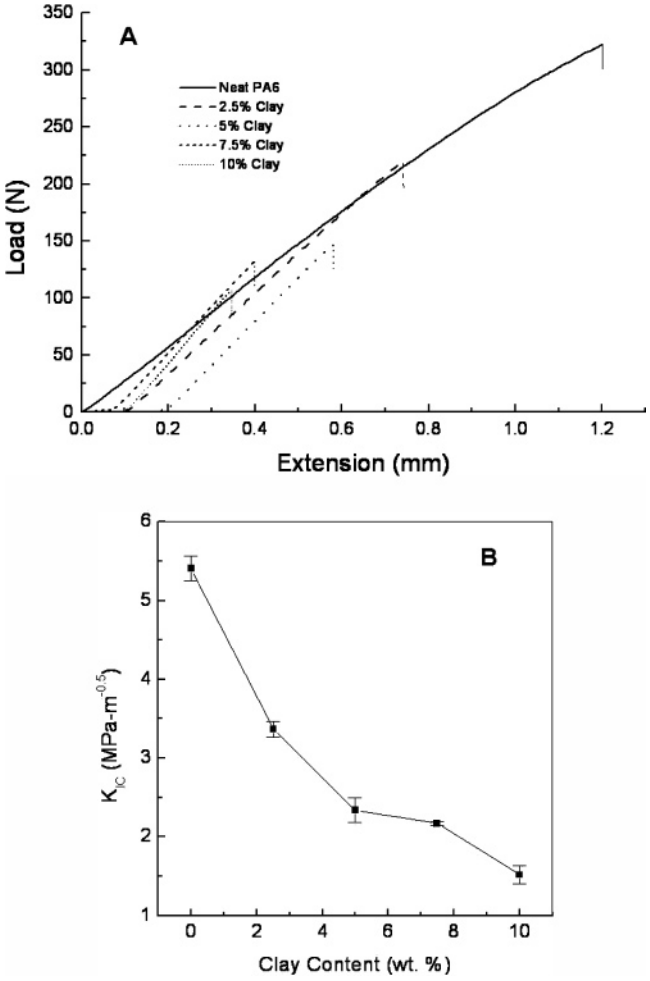

Figure 8. (A) Load−deflection curves for PA-6 nanocomposites with various clay concentrations. (B) Fracture toughness K_{IC} for PA-6 clay nanocomposites with various clay concentrations. The value for PA-6 is nominal because it does not meet linear fracture mechanics criteria. The error bars indicate one standard deviation. 6−7 specimens were used to obtain each data point.

The value for the neat PA-6 should be considered nominal because of the nonlinearity, probably because the crack tip plastic zone was large compared to the specimen dimensions. It can be seen that K_{IC} decreases monotonically as clay content increases. The embrittlement effect is clear and consistent with the stress−strain results.

SEM observations were performed on the fracture surfaces of SEN-3PB samples coated with a thin layer of Au−Pd. The crack initiation region, i.e., just beyond the razor-starter crack, rather than the crack propagation region was the focus of these observations because they are more revealing of the fracture and toughening mechanisms.[45] SEM exhibits a relatively rough fracture surface characteristic for neat PA-6 (Figure 9A), indicating the occurrence of localized cohesive failure sites—probably crazes (as will be shown later)—that merged just prior to final rupture. Interestingly, the fracture surface of the PA-6/2.5 specimen exhibits a much rougher surface than in PA-6 (Figure 9B). This surface characteristic suggests the occurrence of even more cohesive failure or cavitation events just prior to fracture. But, for the nanocomposite samples with 5% or higher clay concentrations, the fracture surfaces are quite different from those observed in neat PA-6 and PA-6/2.5 specimens (Figure 9C,D). These surfaces are still rough, but the roughness is on a finer scale than those with lower clay content, suggesting that the cohesive failure events

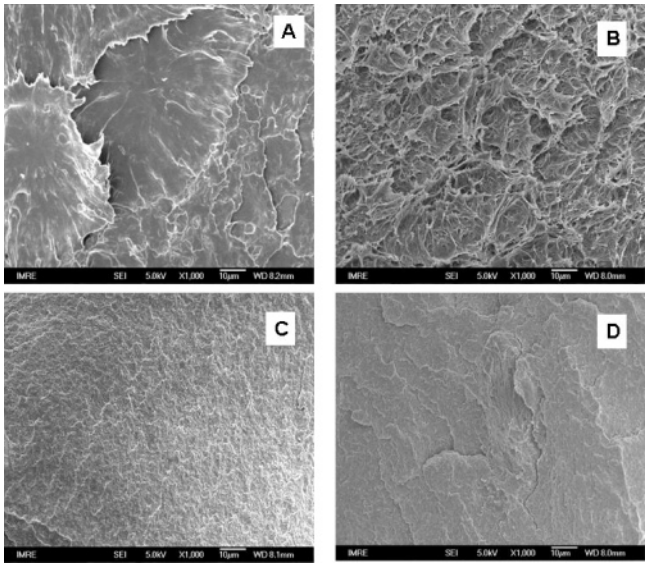

Figure 9. SEM micrographs of fracture surfaces of PA-6 nanocomposites with various clay concentrations: (A) PA-6, (B) PA-6/2.5, (C) PA-6/5, and (D) PA-6/10.

were more numerous and may not have had the opportunity to develop fully before final rupture set in.

3.6. TOM Observations on DN-4PB Specimens. DN-4PB tests[31] were performed on PA-6 and PA-6/clay nanocomposites to study their fracture mechanisms in terms of the development of a damage or process zone (Figure 10).

For neat PA-6, bright-field TOM micrograph shows that multiple cracking or crazing occurred upon fracture (Figure 10A). In PA-6/2.5, TOM shows a small damage zone with a high density of cracks or crazes at the crack tip (Figure 10B). This damage zone is found to be populated by crazes by TEM (Figure 11), although SAXS results (see below) show that the real picture is more complicated.

Surprisingly, for samples with even higher clay concentrations (≥5 wt %), the crack tip damage zone became too small to be observed (Figure 10C,D). The cracks propagated in a straight line in such materials. Under TOM using crossed polars, no sign of birefringence could be detected at any clay level. Thus, the TOM results suggest the occurrence of different fracture mechanisms at different clay loading levels although none involve substantial shear plasticity which would have given rise to observable birefringence. The sizes of the damage zones in the nanocomposites are consistent with the toughness values; viz., PA-6/2.5 has the highest fracture toughness and the largest process zone, followed by nanocomposites with increasing clay loadings but decreasing toughness and process zone size.

3.7. Microdeformation Mechanisms. The stresses at the crack tips of 3PB or 4PB specimens are rather complicated due to the constraint that exists at the crack tip and the subsequent development of fracture mechanisms during deformation. Uniaxial tension, in contrast, subjects the specimen to a simple state of stress during the early stages of deformation before necking set in. The tensile specimens were therefore interrogated by SAXS during and after deformation (but before necking occurred) in order to learn more about the microscopic processes that operate under simple tension. In particular, known cohesive failure mechanisms such as microcracking or crazing were studied.

When subjected to deformation, crazing may occur in many semicrystalline polymers. Crazing is both a mechanism for energy absorption and a cause for the failure of polymers.[46,47] Formation of crazes and the resultant craze concentration are

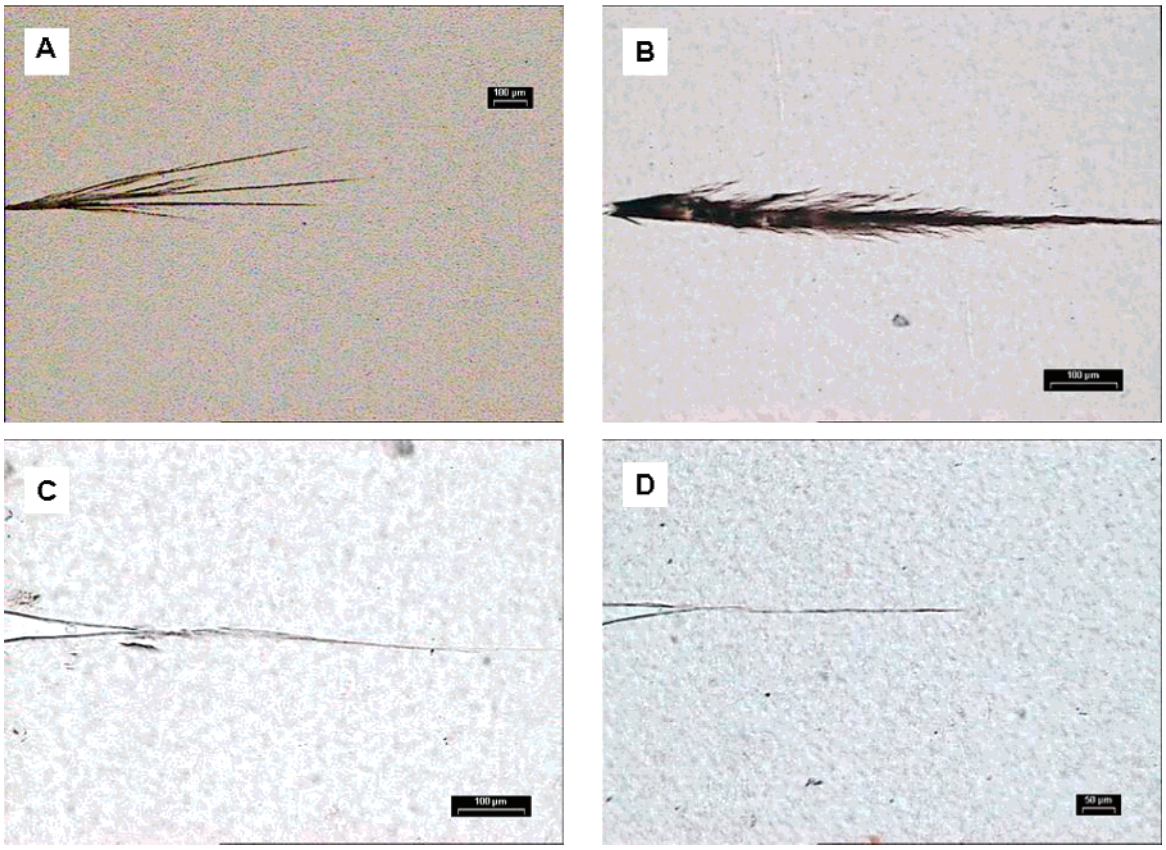

Figure 10. TOM observations of DN-4PB specimens as a function of clay concentration: (A) PA-6, (B) PA-6/2.5, (C) PA-6/5, and (D) PA-6/10. Cracks propagated from left to right.

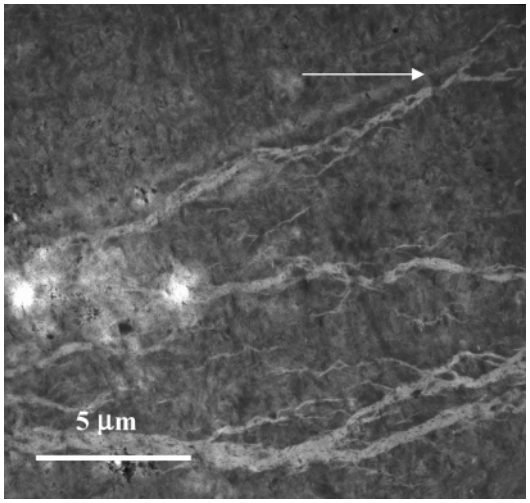

Figure 11. TEM from the crack tip process zone in a PA-6/ 2.5 specimen tested in DN-4PB. Crazes can be readily seen. The arrow indicates the direction of crack propagation.

critical to the mechanical behavior of a polymer. If a polymer system can generate a massive number of crazes during deformation, then a tough polymer may result. On the other hand, crazes could also lead to early and low-energy failure of polymers when only a small density of crazes is generated; in this case the polymer would fail in a brittle manner due to the premature breakdown of a few crazes.

Many methods could be used to probe the craze morphology of polymers. Among them, SAXS is a particularly good technique for quantifying the dimensional characteristics of crazes.[48] In this technique, sample preparation is simple, and the information obtained represents an average over a significant

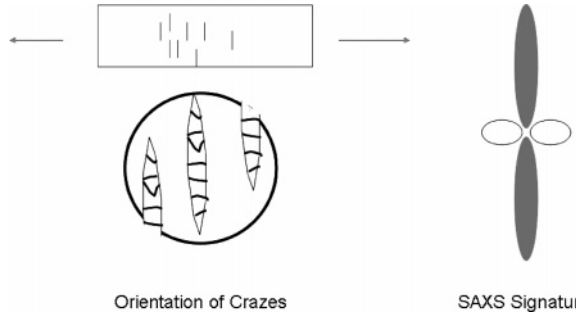

Figure 12. Schematic of craze orientation with respect to the tensile axis and the expected scattering signature from SAXS. In this schematic the X-ray beam is perpendicular to the tensile axis. The injection direction is parallel to the tensile axis.

volume, typically 10^5 mm^3. As shown in Figure 12, if the tensile deformation direction is horizontal, the SAXS pattern from crazes would resemble a narrow vertical strip with two lobes. This meridional scattering is attributed to scattering from fibrils in the crazes,[48] which can be quantitatively related to craze concentration through invariant analysis as follows:

$$Q_r = \sum_{q_1}^{q_2} I(q) q \Delta q + Q_{tail}$$

$$Q_{tail} = \int_{q_2}^{\infty} I(q) q \, dq = \int_{q_2}^{\infty} \frac{K}{q^3} q \, dq = \frac{K}{q_2}$$

where K is the slope according to the Porod analysis, Q_r is a relative invariant, q is the scattering vector, and $I(q)$ is the scattering intensity from craze. On the basis of this equation, the possible formation of crazes during deformation can be probed.

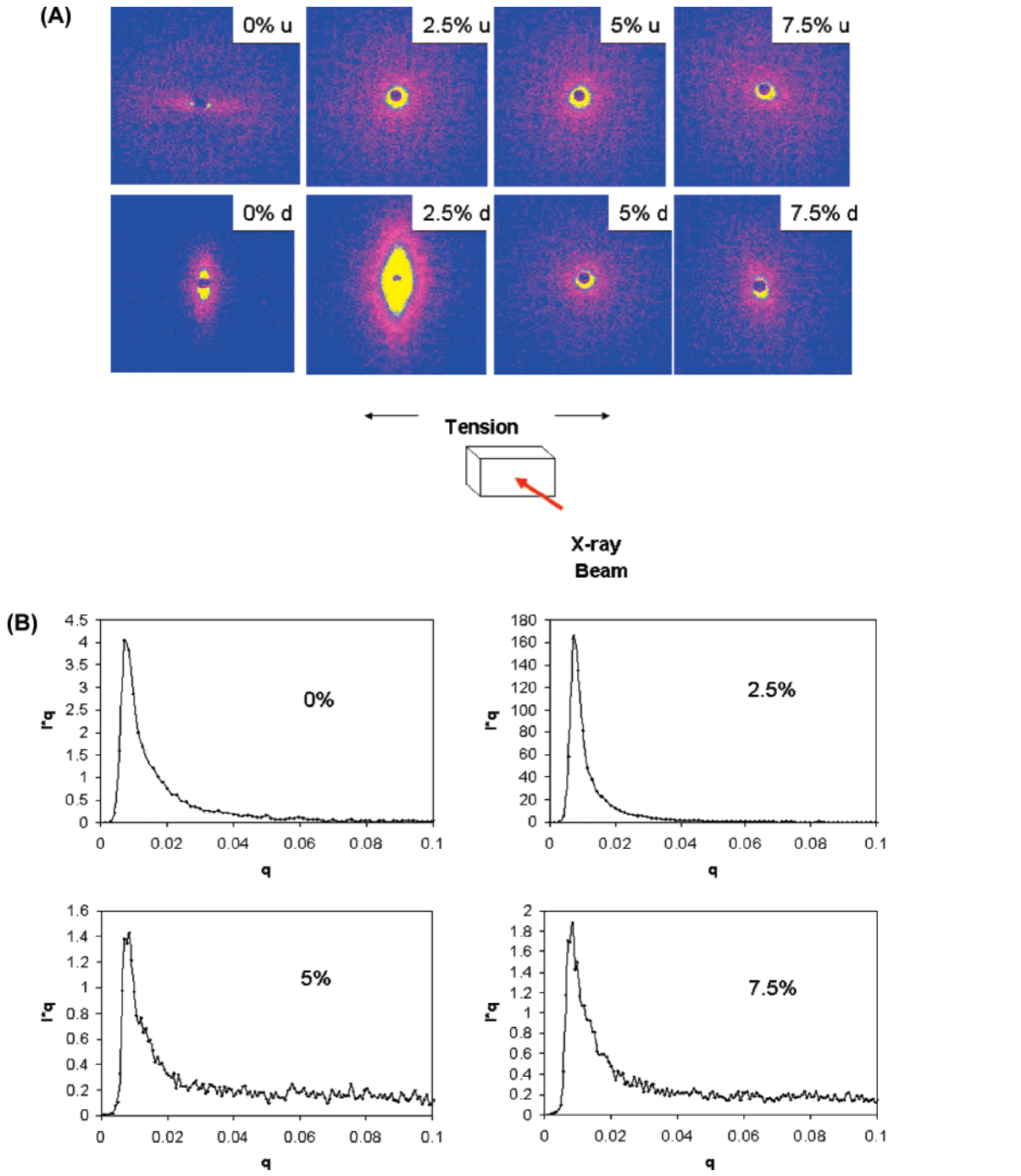

Figure 13. (A) SAXS patterns for PA-6 clay nanocomposites with various clay concentrations. The % indicates wt % of clay. The letter "u" denotes undeformed specimens while "d" denotes deformed specimens. (B) Integrated intensity (Iq) vs scattering vector q from deformed PA-6 clay nanocomposite specimens with various clay concentrations, where $q = 4\pi \sin(\theta)/\lambda$ (1/Å) and Iq = count/s. Note that the Iq scale for each composition is different. The intensity for PA-6/2.5 is particularly high.

For neat PA-6, SAXS detected a small amount of crazing after yield. For PA-6 containing 2.5 wt % of clay, the craze concentration was significantly higher, as shown in Figure 13A.

Note that the SAXS for the deformed specimens was obtained after the specimen had been strained to failure. The SAXS is from a section parallel to the tensile axis; thus, the craze planes are parallel to the X-ray beam. When integrating the scattering intensity along the meridian as shown in Figure 13B, the total intensity for PA-6/2.5 was found to be about 40 times that of neat PA-6. This was probably because the clay platelets acted as craze nucleation sites. When the clay concentration increased further, i.e., 5 and 7.5 wt %, the polymer nanocomposites failed without generating significant crazing. In fact, SAXS hardly registered any craze signature, as shown in Figure 13A. By integrating the scattering intensity along the meridian as shown in Figure 13B, the total intensity is seen to be less than that of neat PA-6 and is only a tiny fraction (1%) of that in PA-6/2.5.

The relative invariants for the neat PA-6 and PA-6 /2.5, PA/5 and PA/7.5 are 0.86, 10.1, 0.13, and 0.10, respectively, according to the above equation, indicating that the craze concentration is the highest for the nanocomposite containing 2.5 wt % clay. For nanocomposites containing 5 and 7.5 wt % clay, the craze concentration is even lower than that in neat PA-6. This could be because the crazes could not fully develop before the

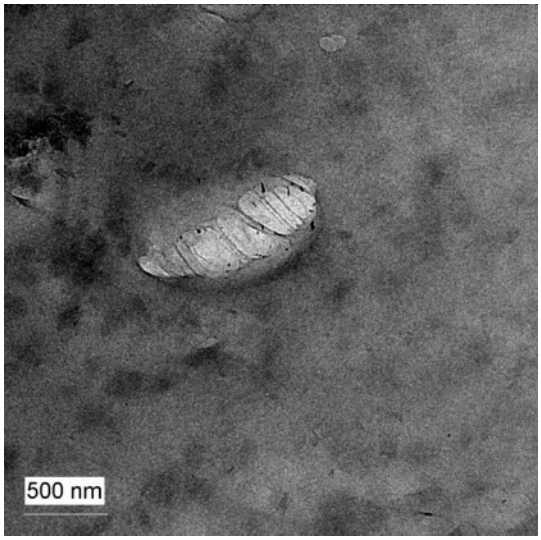

Figure 14. TEM micrograph shows crazes initiated at the interface between clay and matrix.

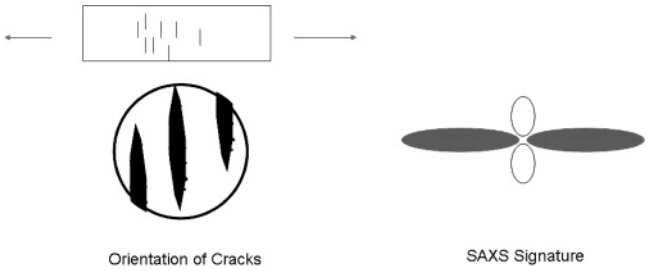

Figure 15. Schematic of microcrack orientation with respect to the tensile axis and the expected scattering signature from SAXS. In this schematic the X-ray beam is parallel to the tensile stress axis.

specimens ruptured; this possibility was verified in another SAXS experiment that will be described below.

The effect of clay on craze concentration and the subsequent deformation behavior of the nanocomposite can be explained by the interplay between craze nucleation and their transformation into microcracks. TEM showed that craze nucleation occurred near the interface between the clay platelets and the polymer matrix (Figure 14**)**.

Consequently, the number of craze nucleation sites increased with clay content. When the number of nucleation sites was small, each craze nucleus was able to fully develop into a long mature craze, such as those shown in the TEM in Figure 11. Such crazes would eventually become a crack upon continued deformation. On the other hand, if the number of nucleation sites was large, the simultaneous development of many crazes would have caused the specimen deforming in bending to become unstable because the compliance would have increased rapidly. The large increase in strain at a given stress level would have caused the crazes to transform into cracks without growing fully along the craze planes. This scenario is consistent with the observations in this work. Specifically, in the case of PA-6/2.5, the number of nucleation sites was apparently large enough to produce a large number of crazes in the process zone, but not so large as to cause the premature transformation of crazes into cracks. With further increase in clay, i.e., to 5 or 7.5 wt %, the rapid increase in the number of crazes apparently caused the crazes to transform quickly into microcracks. This scenario finds support in the SAXS study described in the following.

3.8. SAXS Study of Microcracking. Similar to crazing, cracking is a source of energy absorption as well as cause for failure.[50] However, cracking not accompanied by plastic deformation dissipates only surface energy, while crazing is itself a form of plastic deformation, which absorbs far more energy than cracks of the same length. The development of a process zone with numerous stable microcracks may, however, generate a "crack wake effect" that can improve crack growth resistance.[50] It is therefore important to determine whether significant microcracking had occurred, especially in the crack wake. Cracks are very difficult to detect using SAXS as the length scale of a typical microcrack is well in excess of the range of the SAXS apparatus used in this work, which is normally able to detect scattering centers up to about 80 nm in size. Nevertheless, if the crack width is small, i.e., not yet well developed, it can be detected by the SAXS system used. The characteristics of the microcracks would manifest itself in SAXS as equatorial scattering lobes. Figure 15 shows a schematic of the expected SAXS pattern from microcracks.

For a polymer specimen under tension, microcracks must develop with their crack planes perpendicular to the tensile axis. The crack length along the microcrack propagation direction (i.e., perpendicular to the tensile stress direction) is normally too large to be detected by SAXS.

Fractured samples were studied in directions perpendicular and parallel to the tensile axis using SAXS, and the results are summarized in Figure 16.

SAXS was obtained from a section taken perpendicular to the tensile axis. The scattering in the direction perpendicular to the tensile axis has been discussed previously: it is due to

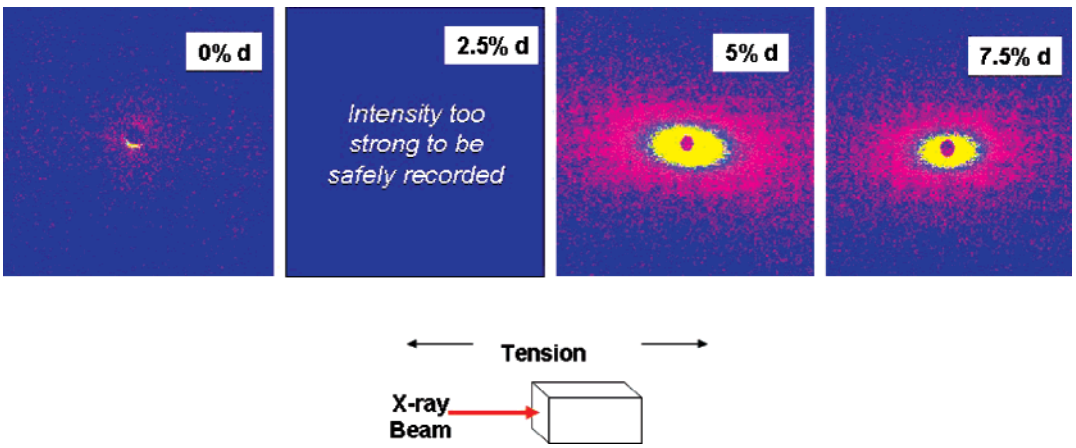

Figure 16. Geometry and signatures of SAXS for PA-6 clay nanocomposites with various clay concentrations under tensile deformation. The % indicates wt % of clay. The letter "d" denotes deformed specimens.

scattering from crazes in the polymer samples and arises from the density fluctuation between the craze fibrils in the crazes.[48] No significant microcrack formation was found in this direction, as the scattering mainly was concentrated on the meridian. By contrast, in the direction *parallel* to the tensile axis, equatorial scattering with reasonable intensity was found for nanocomposites PA-6/5 and PA-6/7.5. The SAXS scattering for PA-6/2.5 in the direction parallel to the tensile axis was so intense that the image could not be recorded safely in the XRD system used. As a result, the data for this composite is not listed here. For neat PA-6, there was no such equatorial scattering.

The equatorial scattering demonstrates the existence of density fluctuation along the tensile direction. This scattering is probably the result of microcracking in the polymer samples with the crack planes perpendicular to the tensile stress. It is reasonable to surmise that the appearance of such scattering can be attributed to the addition of clay that induced cracks. Moreover, it was shown in the TEM results that cracks occurred near the interface between the polymer matrix and the exfoliated clay and/or within the gallery of intercalated clays. The fact that in neat PA-6 no such equatorial scattering was observed lends further credence to this interpretation of the SAXS results.

4. Discussion and Conclusions

The work presented here is the first systematic study of the microscopic fracture mechanisms of PA-6/nanoclay composites despite the fact that such materials have been discovered and studied for over 20 years.[13,15] Similar to what other researchers found, the tensile modulus and yield strength increased with increasing clay concentration, while the strain at yield and at break decreased.[10,11,16−19] Although the addition of nanosized clay platelets in the nanocomposites favors the formation of the γ-form crystal, which is more ductile, the presence of clay, rather than the crystalline form, appeared to play a dominant role in influencing the tensile behavior of the nanocomposites. The fracture toughness measurements show that the normally tough thermoplastic PA-6 is embrittled by the addition of nanoclay. The negative effect on toughness arising from the addition of organoclay apparently overwhelms whatever positive effect there might be from the crystal transformation of the matrix to the more ductile form.

The brittle behavior of PA-6 nanoclay composites may arise from several major factors, which can be categorized as either intrinsic or extrinsic. Intrinsic factors could include degradation of molecular weight due to high compounding temperature, which would favor the formation of cracks, while poor dispersion of clay in the polymer matrix would be another important extrinsic factor. No degradation of molecular weight was found, however. Although the dispersion of clay was not completely uniform, it did not appear to have been the major cause for brittleness, contrary to early expectations. Microdeformation mechanisms such as crazing and microcracking appeared to have been the most important deformation events. SEM observations show a much rougher fracture surface for the PA-6/2.5 sample, which is significantly different from those observed in neat PA-6 and other systems with higher clay contents. TOM and TEM observations indicate that crazing is the main toughening mechanism prior to fracture when clay loading is at 2.5 wt %. SAXS results confirm that at 2.5 wt % clay multiple crazing was the dominant mechanism, while at higher clay contents microcracking appeared to have prevented the crazes from fully developing. Instead, these microcracks linked up and caused rupture of the specimen before significant process zones could form.

The role of the clay platelets apparently was to trigger the formation of numerous crazes, as observed by TEM and corroborated by SAXS. At high clay loadings, microcracks formed near the interface between the clay platelets and the polymer matrix. The good dispersion of the nanoclay and the fact that the microcracks did not occur directly at the clay surface suggest that clay−polymer adhesion was adequate. Instead, the low cohesive strength of PA-6, an intrinsic property of the polymer which made possible the easy formation of crazes and ready transformation into microcracks, was apparently the chief culprit in the brittleness of PA-6/clay nanocomposites.

It should be noted that PA-6 without any clay was the toughest material in the present study. The addition of as little as 2.5% clay was sufficient to cause embrittlement, although some other desirable properties were improved. The ideal material, as is often the case, depends on the application that it will be put to.

It is worthwhile to point out that literature data on basic mechanical properties of both conventional fiber- or particulate-filled composites and nanocomposites vary considerably because of the differences in polymers, additives, and processing conditions used. For example, even the reported modulus for glass-fiber-filled PA-6 could vary by several hundred percent, depending on the commercial grade and the producer. In the case of nanocomposites the exfoliating agent, surfactant, coupling agent, etc., could also significantly influence mechanical properties. (This is also true for conventional composites, but the effect might not be as large.) For these reasons the absolute values of mechanical properties presented in this paper are perhaps not as important as the underlying microdeformation mechanisms and the causes for embrittlement. With a different PA-6/nanoclay composite an ideal clay content for toughness might be different from 2.5 wt %. The importance of the mechanisms described in this work lies perhaps in their generic nature.

It is also interesting to note that in conventional particulate-filled composites poor adhesion between the filler and the matrix is often blamed for lower than desired mechanical performance. In the present work adhesion between the inorganic and organic phases appears not to be the issue. Rather, the failure initiation sites appear to be in the matrix, though adjacent to the clay. This observation suggests that the fundamental cohesive strength of polymers may have been reached in well-exfoliated nanocomposites.

Acknowledgment. The authors thank the AOARD Tokyo Office of the US Air Force Office of Scientific Research and the Institute of Materials Research and Engineering (IMRE) in Singapore for their financial support of this work.

References and Notes

(1) Lan, T.; Kaviratna, P. D.; Pinnavaia, T. J. *Chem. Mater.* **1994**, *6* (5), 573−575.
(2) Giannelis, E. P. *Adv. Mater.* **1996**, *8* (1), 29−35.
(3) Yano, K.; Usuki, A.; Okada, A.; Kurauchi, T.; Kamigaito, O. *J. Polym. Sci., Polym. Chem.* **1993**, *31* (10), 2493−2498.
(4) Shi, H. Z.; Lan, T.; Pinnavaia, T. J. *Chem. Mater.* **1996**, *8* (8), 1584−1587.
(5) Zhu, J.; Start, P.; Mauritz, K. A.; Wilkie, C. A. *Polym. Degrad. Stabil.* **2002**, *77* (2), 253−258.
(6) Massam, J.; Wang, Z.; Pinnavaia, T. J.; Lan, T.; Beall, G. *Abstr. Pap. Am. Chem. Soc.* **1998**, *215*, U344−U344.
(7) Wang, K.; Chen, L.; Wu, J. S.; Toh, M. L.; He, C. B.; Yee, A. F. *Macromolecules* **2005**, *38* (3), 788−800.
(8) Lan, T.; Wang, Z.; Shi, H. Z.; Pinnavaia, T. J. *Abstr. Pap. Am. Chem. Soc.* **1995**, *210*, 157−157.
(9) Lan, T.; Pinnavaia, T. J. *Chem. Mater.* **1994**, *6* (12), 2216−2219.

(10) Liu, L. M.; Qia, F.; Zhu, X. G.; Qi, Z. G.; Chen, G. Q. *Acta Polym. Sin.* **1998**, *(3)*, 304−310.
(11) Cho, J. W.; Paul, D. R. *Polymer* **2001**, *42* (3), 1083−1094.
(12) Gam, K. T.; Sue, H. J. *Abstr. Pap. Am. Chem. Soc.* **2000**, *219*, U498−U498.
(13) Kojima, Y.; Usuki, A.; Kawasumi, M.; Okada, A.; Fukushima, Y.; Kurauchi, T.; Kamigaito, O. *J. Mater. Res.* **1993**, *8* (5), 1185−1189.
(14) Usuki, A.; Kojima, Y.; Kawasumi, M.; Okada, A.; Fukushima, Y.; Kurauchi, T.; Kamigaito, O. *J. Mater. Res.* **1993**, *8* (5), 1179−1184.
(15) Usuki, A.; Kojima, Y.; Kawasumi, M.; Okada, A.; Kurauchi, T.; Kamigaito, O. *Abstr. Pap. Am. Chem. Soc.* **1990**, *200*, 218-Poly.
(16) Ranade, A.; D'Souza, N. A.; Gnade, B.; Dharia, A. *J. Plast. Film Sheeting* **2003**, *19* (4), 271−285.
(17) Xie, S. B.; Zhang, S. M.; Liu, H. J.; Chen, G. M.; Feng, M.; Qin, H. L.; Wang, F. S.; Yang, M. S. *Polymer* **2005**, *46* (14), 5417−5427.
(18) Tsai, J. L.; Huang, J. C. *J. Compos. Mater.* **2006**, *40* (10), 925−938.
(19) Dasari, A.; Yu, Z. Z.; Mai, Y. W.; Hu, G. H.; Varlet, J. L. *Compos. Sci. Technol.* **2005**, *65* (15−16), 2314−2328.
(20) Fornes, T. D.; Yoon, P. J.; Keskkula, H.; Paul, D. R. *Polymer* **2001**, *42* (25), 9929−9940.
(21) Lincoln, D. M.; Vaia, R. A.; Wang, Z. G.; Hsiao, B. S.; Krishnamoorti, R. *Polymer* **2001**, *42* (25), 9975−9985.
(22) Weon, L.; Sue, H. J. *J. Polym. Sci., Polym. Phys. Ed.* **2005**, *43*, 3555−3566.
(23) Paul, D. R.; Yoon, P. J.; Fornes, T. D. *Abstr. Pap. Am. Chem. Soc.* **2002**, *224*, U426−U426.
(24) Wang, S. F.; Hu, Y.; Li, Z. L.; Wang, Z. Z.; Zhuang, Y. L.; Chen, Z. Y.; Fan, W. C. *Colloid Polym. Sci.* **2003**, *281* (10), 951−956.
(25) Liu, X. H.; Breen, C. *Macromol. Rapid Commun.* **2005**, *26* (13), 1081−1086.
(26) Liu, L. M.; Qi, Z. N.; Zhu, X. G. *J. Appl. Polym. Sci.* **1999**, *71* (7), 1133−1138.
(27) Tung, J.; Gupta, R. K.; Simon, G. P.; Edward, G. H.; Bhattacharya, S. N. *Polymer* **2005**, *46* (23), 10405−10418.
(28) Dasari, A.; Yu, Z. Z.; Hu, G. H.; Varlet, J.; Mai, Y. W. *Abstr. Pap. Am. Chem. Soc.* **2005**, *230*, U3563−U3564.
(29) Garcia, M.; de Rooij, M.; Winnubst, L.; van Zyl, W. E.; Verweij, H. *J. Appl. Polym. Sci.* **2004**, *92* (3), 1855−1862.
(30) Wei, G. X.; Sue, H. J.; Chu, J.; Huang, C. Y.; Gong, K. C. *J. Mater. Sci.* **2000**, *35* (3), 555−566.
(31) Sue, H. J.; Yee, A. F. *J. Mater. Sci.* **1993**, *28*, 2915−2919.
(32) da Silveira, N. P.; Ehrburger-Dolle, F.; Rochas, C.; Rigacci, A.; Pereira, F. V.; Westfahl, H. *J. Therm. Anal. Calorim.* **2005**, *79* (3), 579−585.
(33) Okamoto, M.; Morita, S.; Kotaka, T. *Polymer* **2001**, *42* (6), 2685−2688.
(34) Sun, L.; Boo, W. J.; Browning, R. L.; Sue, H.-J.; Clearfield, A. *Chem. Mater.* **2005**, *17* (23), 5606−5609.
(35) Sue, H. J.; Gam, K. T.; Bestaoui, N.; Spurr, N.; Clearfield, A. *Chem. Mater.* **2004**, *16* (2), 242−249.
(36) Boo, W. J.; Sun, L.; Liu, J.; Moghbelli, E.; Clearfield, A.; Pham, H.; Verghese, N.; Sue, H.-J. *J. Polym. Sci., Polym. Phys. Ed.* **2007**, *45*, 1459−1469.
(37) Fornes, T. D.; Yoon, P. J.; Hunter, D. L.; Keskkula, H.; Paul, D. R. *Polymer* **2002**, *43* (22), 5915−5933.
(38) Fornes, T. D.; Paul, D. R. *Polymer* **2003**, *44* (14), 3945−3961.
(39) Shelley, J. S.; DeVries, K. L. *Exp. Mech.* **2002**, *42* (2), 178−181.
(40) Fornes, T. D.; Yoon, P. J.; Paul, D. R. *Polymer* **2003**, *44* (24), 7545−7556.
(41) Fornes, T. D.; Hunter, D. L.; Paul, D. R. *Macromolecules* **2004**, *37* (5), 1793−1798.
(42) Boo, W.-J.; Sun, L.; Liu, J.; Clearfield, A.; Sue, H.-J. *Compos. Sci. Technol.* **2006**, *67*, 262−269.
(43) Lee, J.; Yee, A. F. *J. Appl. Polym. Sci.* **2001**, *79* (8), 1371−1383.
(44) Lee, J.; Yee, A. F. *J. Mater. Sci.* **2001**, *36* (1), 7−20.
(45) Sue, H. J.; Gam, K. T.; Bestaoui, N.; Clearfield, A.; Miyamoto, M.; Miyatake, N. *Acta Mater.* **2004**, *52* (8), 2239−2250.
(46) Kausch, H. H.; Gensler, R.; Grein, C.; Plummer, C. J. G.; Scaramuzzino, P. *J. Macromol. Sci., Phys.* **1999**, *B38* (5−6), 803−815.
(47) Michler, G. H. *Makromol. Chem., Macromol. Symp.* **1991**, *41*, 39−54.
(48) He, C. B.; Donald, A. M.; Butler, M. F.; Diat, O. *Polymer* **1998**, *39* (3), 659−667.
(49) Weon, J. I.; Sue, H. J. *J. Mater. Sci.* **2006**, *41* (8), 2291−2300.
(50) Du, J.; Thouless, M. D.; Yee, A. F. *Acta Mater.* **2000**, *48* (13), 3581−3592.

MA071781S